Toward FBG-Sensorized Needle Shape Prediction in Tissue Insertions

Dimitri A. Lezcano*, Min Jung Kim†, Iulian I. Iordachita*, Jin Seob Kim*

Abstract— **Complex needle shape prediction remains an issue for planning of surgical interventions of flexible needles. In this paper, we validate a theoretical method for flexible needle shape prediction allowing for non-uniform curvatures, extending upon a previous sensor-based model which combines curvature measurements from fiber Bragg grating (FBG) sensors and the mechanics of an inextensible elastic rod to determine and predict the 3D needle shape during insertion. We evaluate the model's effectiveness in single-layer isotropic tissue for shape sensing and shape prediction capabilities. Experiments on a four-active area, FBG-sensorized needle were performed in varying single-layer isotropic tissues under stereo vision to provide 3D ground truth of the needle shape. The results validate a viable 3D needle shape prediction model accounting for non-uniform curvatures in flexible needles with mean needle shape sensing and prediction root-mean-square errors of 0.479 mm and 0.892 mm, respectively.**

Index Terms— **flexible needle; fiber Bragg grating; mathematical model; needle shape detection;**

I. INTRODUCTION

Needle insertion is typical for surgical intervention including biopsy, cryoablation, and injection. To reduce tissue damage and for vital organ obstacle avoidance, asymmetric bevel-tipped flexible needles are commonly used for needle insertion. Asymmetric bevel-tipped flexible needles allow for needle steering as the bevel tip allows for deviations of the needle's trajectory. To properly plan for needle insertions, we must have a method to determine the future needle shape upon further insertion, warranting an accurate needle shape prediction model when for needle insertion.

The unicycle/bicycle model [1], [2] laid the ground work for needle shape determination. Since then, flexible needle steering models have included varying kinematics-based models [1]–[3] and mechanics-based models [4]–[6]. Kinematics-based models have been used in control and planning of the needle, but may not properly capture additional or complex needle deformation. Mechanics-based models are usually based on classical beam theory to determine needle shape, but require detailed information on the tissue. A sensor-based model using a Lie-group theoretic approach [7] has been proven successful for shape-sensing in multi-layer tissue using FBG sensors [8]. This model is based on the theory of elastic rods and Lie groups with the advantage of complex needle shape recognition in 3D space through the use of FBG sensors.

* D. A. Lezcano, I. I. Iordachita, and J. S. Kim are with the Department of Mechanical Engineering, Johns Hopkins University, Baltimore, MD, USA {dlezcan1, iordachita, jkim115}@jhu.edu

† M. J. Kim is with the Department of Biomedical Engineering, Johns Hopkins University, Baltimore, MD, USA mjkim@jhu.edu

Aside from needle shape-sensing, an important issue is the prediction of needle shape during further insertion — an aspect critical in the planning of needle steering into human tissue. For accurate needle insertion path-planning, an experimentally-validated and accurate prediction model is required. In kinematics-based models, prediction of needle insertion trajectory is performed by integrating the kinematic system equation. Methods based on a rapidly-exploring random tree (RRT) have been implemented for needle insertion planning using kinematic models [9]–[11]. This approach is simple in-practice, however these models are usually founded upon a constant curvature assumption, limiting the realization of all needle shapes. The Lie-group theoretic model, which treats the needle as an elastic rod with distributed loads allowing for non-uniform and complex curvatures, has the potential to enable more accurate needle shape prediction. In prior work, we extended this shape-sensing theoretical framework to accommodate needle shape prediction in single- and multi-layer tissue [12].

In this paper we evaluate our novel needle shape prediction model in varying single-layer homogeneous tissues, using a four-active area needle. In Section II, we present the consideration of FBG-array shape sensors as curvature measurement devices, shape-sensing and shape-prediction models used for a sensorized needle. In Section III we discuss our experimental setup to perform sensorized needle calibration, and validate our needle shape-sensing and shape prediction model in single-layer tissue using 3D position measurements under stereo vision. Following in Section IV we present and discuss our results and conclude the paper. The novelty of this work includes 3D shape reconstruction of a four-active area needle under stereo vision and the evaluation of a novel method to predict 3D needle shapes upon further insertion allowing for non-uniform curvature modelling.

II. METHODS

A. FBG Sensor Model

FBGs are Bragg reflectors inscribed in fiber optic cables which detect strain and temperature shifts by the change in the Bragg wavelength. This change in the peak Bragg wavelength is characterized by Bragg's law and the shift in the Bragg wavelength, $\Delta\lambda$, can be approximated by

$$\Delta\lambda = k_\epsilon \epsilon + k_T \Delta T, \tag{1}$$

where ϵ is the strain induced in the FBG, ΔT is the change in temperature of the FBG, and k_ϵ and k_T are the

characteristic coefficients of the FBG associated with strain and temperature, respectively.

In our FBG-sensorized needle, at each of the active areas, we have three FBGs arranged in a trigonal pattern array ($120°$ relative to each other). In order to measure the effect of strain directly, we remove the effect of temperature by assuming that k_T is the same for all of the FBGs (validated by temperature tests of these FBGs) and by subtracting the mean Bragg wavelength shift from each of the FBGs in the array, we eliminate effects of temperature change on the Bragg wavelength shift. We define this method as *temperature compensation*.

For a rod modelled as an Euler-Bernoulli rod, we can determine the curvature of the rod by

$$\kappa = \frac{\epsilon}{r} \tag{2}$$

where κ is the curvature at some radius r from the rod's center. We can see that, with temperature compensation, $\Delta\lambda \propto \kappa$. We then use a linear model to compute the temperature compensated wavelength shifts from an FBG array, $\overline{\Delta\lambda_i}$ ($i = 1, 2, 3$), and the cross-sectional curvature $\boldsymbol{\omega} = (\kappa_{xz}, \kappa_{yz})^T$ by

$$\boldsymbol{\omega} = \begin{pmatrix} \kappa_{xz} & \kappa_{yz} \end{pmatrix}^T = C \begin{pmatrix} \overline{\Delta\lambda_1} & \overline{\Delta\lambda_2} & \overline{\Delta\lambda_3} \end{pmatrix}^T \tag{3}$$

where $C \in \mathbb{R}^{2\times3}$ is the calibration matrix, determined by the FBG-sensorized needle calibration process referenced in Sec. III-C.

B. Needle Shape-Sensing

The sensor-based Lie-group theoretic model [13] describes the curvature (ω_1 and ω_2 along the local x- and y-axes, respectively) and torsion (ω_3 along the local z-axis) of the needle as

$$\boldsymbol{\omega}(s) = [\omega_1\ \omega_2\ \omega_3]^T = \left(R^T(s)\frac{dR(s)}{ds}\right)^{\vee} \tag{4}$$

where $R(s) \in SO(3)$ denotes the rotation matrix in 3D space describing the orientation of the body-fixed frame attached at each point along the needle. $s \in [0, L]$ denotes the arclength of the needle with total insertion length L. Here $\vee$ operation defines a 3D vector associated with a 3×3 skew-symmetric matrix $R^T\frac{dR}{ds}$ [14].
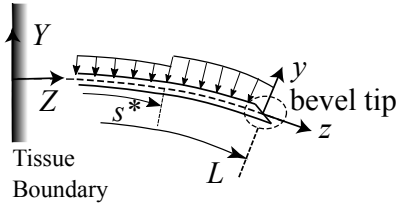

Fig. 1: A schematic of the bevel-tipped needle in the ideal insertion into two-layered tissue, which is modeled as two different uniformly distributed loads (normal components are only shown).

When inserting into tissue, the needle is modeled as an inextensible elastic rod. Under ideal conditions, we assume

that the needle experiences uniformly distributed loads. In case of homogeneous tissue (i.e., single-layer) insertion, a single uniformly-distributed load is assumed. In all cases, due to an asymmetric bevel tip, the needle ideally deforms only in one plane (yz plane in the world frame as shown in Fig. 1), which is captured by introducing the intrinsic curvature $\kappa_0(s)$. For the single-layer case, an intrinsic curvature coefficient, κ_c, is introduced to model the combined effect of the needle's and tissue's mechanical properties on needle bending. Refer to [13] for details. Then the Euler-Poincaré (E-P) equation [15], [16] together with FBG sensor data and an initial deformation at the insertion base, $\boldsymbol{\omega}_{init}$, are used to determine the deformation, $\boldsymbol{\omega}(s)$, and subsequently the needle shape, $\mathbf{r}(s)$, by minimizing the elastic potential energy of the rod.

C. Needle Shape Prediction

To predict the shape of the needle further inserted, we assume the dependence of κ_c on varying insertion lengths. Using a current or previous determined needle shape at a reference insertion length L_{ref}, we can compute the intrinsic curvature at a given insertion length L by computing the coefficients required for the needle shape sensing model: κ_c and $\boldsymbol{\omega}_{init}$. In [12], computing κ_c for increased insertion lengths can be characterized by

$$\kappa_c(L) = \kappa_{c,ref}\left(L_{ref}/L\right)^p, \tag{5}$$

where $\kappa_{c,ref}$ is the determined κ_c at the insertion length L_{ref} and $p = 0.592$ is the proportionality scaling parameter. A similar scaling as (5) is performed for $\boldsymbol{\omega}_{init}$ on a per insertion scenario by

$$\boldsymbol{\omega}_{init}(L) = \boldsymbol{\omega}_{init,ref}\left(L_{ref}/L\right)^q \tag{6}$$

where $\boldsymbol{\omega}_{init,ref}$ is the $\boldsymbol{\omega}_{init}$ determined at L_{ref} and q is the proportionality constant to be optimized through minimizing the predicted deviation of deeper insertions. After determining $\kappa_c(L)$ and $\boldsymbol{\omega}_{init}(L)$, we can then generate $\mathbf{r}(s)$ at insertion depth L by using our shape-sensing model as explained in Section II-B.

III. EXPERIMENT

The goal of the needle insertion experiment presented in this paper is to validate our needle shape-sensing model and shape-prediction model.

A. Experimental Setup

Isotropic gel phantoms are constructed from plastic of various stiffness (Plastic from M-F Manufacturing Company, TX, US) to simulate soft and stiff tissue. To create the stiff tissue, a ratio of 4:1 liquid plastic to plastic hardener was used and to create the soft tissue, no plastic hardener was used. The optical sensing interrogator was used to gather FBG-sensor data and the experiment is visualized under stereo vision. An acrylic box of dimensions allowing for 120mm insertion depths holds the tissue in-place and staples at the insertion side of the gel are implemented to prevent excess tissue deformation at the insertion boundary,
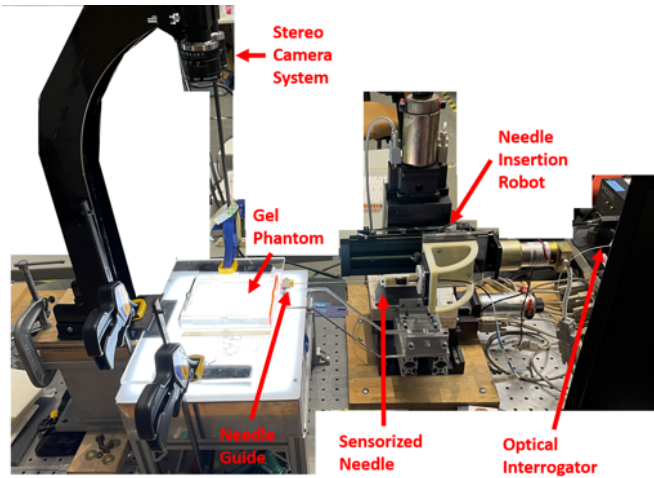
3506

Fig. 2: Needle insertion experimental setup under stereo visualization. Insertion of the needle into the gel phantom is performed.

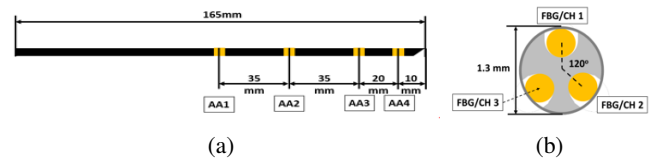(a)   (b)

Fig. 3: The FBG-sensorized needle schematic. (a) The locations of the four-active areas. (b) The orientation of the fiber optic cables in the needle.

C. Needle Characterization and Calibration

Sensorized needle characterization is performed to ensure the assumptions of linearity between the FBG sensor readings and the strain induced in each of the fibers after construction of the needle. During construction of the needle, construction errors can arise from the fiber optic cable twisting inside the grooves of the needle or an improper adherence to the needle at the sensing location. Needle characterization is performed by using an XYZ linear stage (XYR-6060 & LM-400, Dover Motion, Boxborough, MA) robot with a motorized rotary stage (B5990TS, Velmex, Inc., Bloomfield, NY) to rotate the needle about its axis. At the tip of the needle, deflections are induced at $\leq 10\%$ to remain in an Eulerian approximation of strain induced in the needle. Five trials are performed for three different rotation angles (0, 120 and -120°) at 10 deflections at the tip recording 200 FBG signal shifts per deflection loading and unloading the beam. The three different rotation angles are aimed to maximize the strain induced in each of the fibers individually.

Needle calibration was performed using constant curvature jigs (one for calibration and one for validation) to map the temperature compensated wavelength shifts at each of the sensing locations in the sensorized needle. Fig. 4 illustrates the experimental setup for the sensorized needle calibration. Two 3D printed jigs (material ABS, Stratasys F170 printer) with a total of 13 distinct curvatures ranging from 0 to $4\mathrm{m}^{-1}$ were used to induce constant curvatures in the four-active areas along the needle. These grooves were filled with 16G needles for the needle to be inserted into, reducing human error of needle orientation when placing the needle into the grooves. We gathered the FBG signal responses using a Micron Optics Hyperion si155 optical sensing interrogator, providing a wavelength resolution of 1pm.
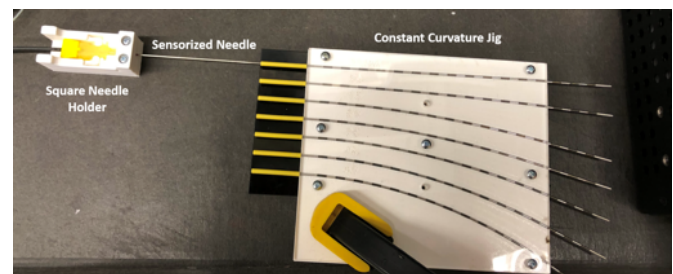
simulating the clinician stretching the tissue during initial insertion. A 3D printed needle holder is attached to a manual rotary stage installed on a 4-degree of freedom linear stage to perform the needle insertion. A custom 18G needle guide is attached to the base of the needle insertion robot listed in Fig. 2 to ensure that insertions into the phantom tissue is nearly perpendicular to the tissue boundary.

For each of the tissues, nine insertion trials are performed for insertion depths of 110, 115 and 120 mm. These insertion depths are chosen to ensure that all four of the active areas are reliably in the tissue to have accurate sensor readings at the needle's sensing locations. At each of the insertion depths, a stereo image pair is taken along with 200 wavelengths per FBG sensor, along with a reference image pair prior to needle insertion and 200 unstrained reference wavelengths per FBG sensor of a straight needle. The collected wavelengths are averaged, subtracted from the unstrained Bragg wavelengths and temperature compensated to incorporate in the shape-sensing model and determine the 3D needle shape from the FBG-sensor readings. The stereo pair of images is used to reconstruct the 3D needle shape inserted into the box. The tip of the needle is used as a feature point to align the two needle shapes, as it is reliably segmented and matched in the stereo image pair and a point-cloud registration is performed on the overlapping needle insertion shapes. At each insertion depth, the needle shape is predicted at the future insertion depths (i.e. 110 mm predicts 115 and 120 mm, and 115 mm predicts 120 mm).

B. FBG-Sensorized Needle

We built a four-active area FBG-sensorized needle where the FBG sensing arrays are placed in a trigonal pattern (120° relative angle) at the sensing locations of 10, 30, 65 and 100 mm from the tip of an 18G nitinol MRI-compatible needle (type KIM18/20, Innovative Tomography Products GmbH, Germany), as shown in Fig. 3.

Fig. 4: Needle calibration using constant curvature jig setup.

For calibration the needle was bent in the xz and yz planes referenced in Fig. 1, inserted into the each of the constant

curvature grooves five times for four different orientations at angles $90°$ from each other ($0°, 90°, 180°$, and $-90°$). The calibration matrices, C, for each active area from (3) are then determined by a weighted least squares problem where non clinically-relevant curvatures ($> 1m^{-1}$) are weighted 1/20th the weight of the clinically-relevant curvatures ($\leq 1m^{-1}$) [17]. The 12 non-zero curvatures are partitioned into a calibration and validation datasets to determine the validity of our calibration. After performing curvature calibration, reliability weightings, w_i, are given to each of the four-active areas such that $\sum_{i=1}^{4} w_i = 1$, and that $\{w_i\}$ are to optimize the deviation needle's determined shape from FBG measurements from ground truth in the constant curvature cases. These weightings allow for optimal shape-sensing capabilities given our model. The calibration errors of this needle's shape-sensing capabilities are given by an mean RMSE of 0.196mm for all the clinically-relevant curvatures.

D. Stereo Vision Ground Truth

To determine the 3D ground truth needle shape when inserting into tissue, two identical cameras, listed in the experimental setup, were used for stereo vision of the needle. The resolution of each camera is 1024×768 pixels. Stereo camera calibration is performed to remove distortion and determine the stereo camera setup's intrinsic and extrinsic parameters. The 3D needle shape is determined by an initial segmentation of the needle's centerline in the two images using a reference (no needle present) stereo image pair. After the initial segmentation is performed, stereo image rectification is performed, followed by smoothing and inter-polating the centerlines using second order B-splines. Stereo matches are determined by template matching at each of the centerline points along the epipolar lines on resized images by $2.5\times$, and are smoothed and interpolated by second order B-splines. Finally the interpolated stereo matches are used to reconstruct the 3D needle shape using triangulation.

The aforementioned method is tested on needles inserted into the constant curvature jigs and it is found to have a mean 3D reconstruction error of 0.160 ± 0.0545mm. Trans-formation of the stereo reconstructed shape into the needle's coordinate frame is performed by a point-cloud registration for comparison of the stereo reconstructed shapes.

IV. RESULTS

Tissue stiffness was measured with an OO durometer (ASTM 2240, MXBAOHENGus Instrument Co., China) and the two tissue stiffnesses tested were given by 20 units and 36 units for the soft and stiff tissue, respectively. For each insertion depth, we determine the insertion parameters κ_c and ω_{init}, listed in Section II-B, by optimizing these parameters in our model relative to our sensor's curvature measurements. For needle shape prediction, the current needle shape param-eters are kept fixed and q is optimized in (6) to minimize predicted deviation. Finally (5) and (6) are used to determine the shape-sensing parameters at the predicted insertion depth and are then used to predict the needle shape.

TABLE I: Mean shape-sensing errors between the FBG-determined needle shape and the stereo reconstructed ground truth for each tissue stiffness.

Tissue Stiffness	RMSE (mm)	IPE (mm)	OPE (mm)
20 (Soft)	0.473 ± 0.195	0.220 ± 0.107	0.159 ± 0.074
36 (Stiff)	0.486 ± 0.233	0.172 ± 0.116	0.248 ± 0.164

TABLE II: Mean shape errors between the FBG-predicted needle shape and the stereo reconstructed ground truth for each tissue stiffness.

Tissue Stiffness	RMSE (mm)	IPE (mm)	OPE (mm)
20 (Soft)	0.810 ± 0.217	0.659 ± 0.081	0.623 ± 0.165
36 (Stiff)	0.975 ± 0.497	0.663 ± 0.128	0.752 ± 0.379

We consider three types of 3D shape error metrics: root-mean-square-error (RMSE), in-bending-plane (yz) error (IPE) and out-of-bending-plane (xz) error (OPE). RMSE is used to characterize overall shape correspondence, IPE is used to determine the error in the natural bending plane of the bevel-tipped needle and OPE is used to determine the errors associated with deflections out of the natural bending plane of the bevel-tipped needle. RMSE is defined between two 3D needle shapes $\{\mathbf{r}_1(s_i)\}_{i=1}^{N}$ and $\{\mathbf{r}_2(s_i)\}_{i=1}^{N}$ as

$$RMSE = \sqrt{\frac{1}{N}\sum_{i=1}^{N}||\mathbf{r}_1(s_i) - \mathbf{r}_2(s_i)||^2} \qquad (7)$$

where s_i is the parameterized arclength of each of the two needle shapes. The IPE is defined as

$$IPE = \frac{1}{N}\sum_{i=1}^{N}\left\|\begin{pmatrix}0 & 1 & 1\end{pmatrix} \cdot ((\mathbf{r}_1(s_i) - \mathbf{r}_2(s_i))\right\|. \qquad (8)$$

Similarly, OPE is defined as

$$OPE = \frac{1}{N}\sum_{i=1}^{N}\left\|\begin{pmatrix}1 & 0 & 1\end{pmatrix} \cdot ((\mathbf{r}_1(s_i) - \mathbf{r}_2(s_i))\right\|. \qquad (9)$$

We first present the needle characterization results to validate our assumptions of the FBG signal response with respect to the strain and curvature induced on the needle. In Fig. 5, we see that the response in the four active areas imply a linear relationship with the deflection, and within an Eulerian approximation, the induced strain. Furthermore, signal response in the active areas are larger at active areas further from the tip, justifying our decision to use reliability weightings discussed in Section III-C. Given that our FBG signals respond linearly with induced strain in the fiber, we have from (2) that the constructed needle's signals respond linearly with the curvature, confirming an acceptable construction of the FBG sensorized needle. =

To validate our shape-sensing method, we present our shape sensing errors in Fig. 7a and Table I. We find that RMSE reconstruction errors between both tissues is 0.479 ± 0.213mm, indicating good shape-sensing capabilities. An example of the stereo reconstruction is presented in Fig. 6 where the 3D needle shapes at an insertion depth of 120mm,

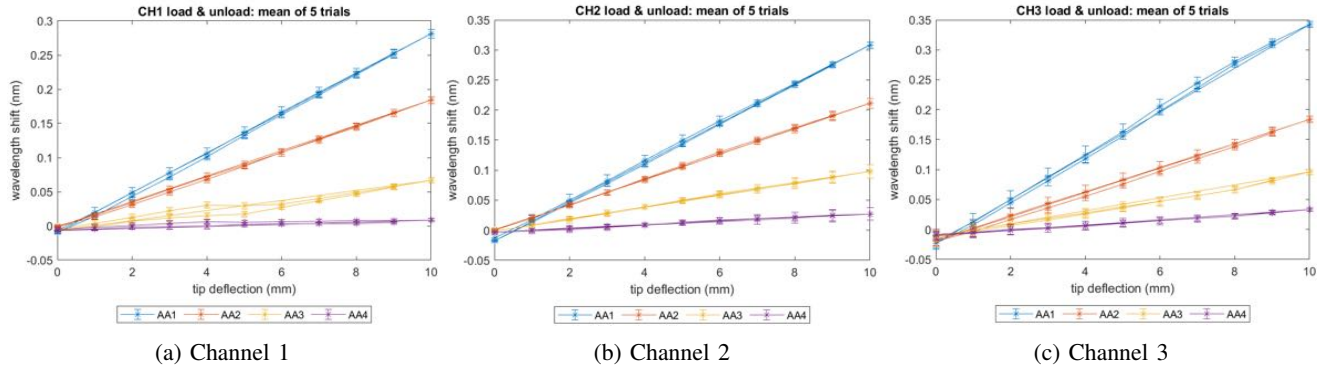|		
(a) Channel 1	(b) Channel 2	(c) Channel 3

Fig. 5: Averaged FBG signal response with respect to the tip deflections over each of the three different needle rotation angles for loading and unloading of the needle.

(a) 3D needle shapes, soft tissue	(b) 3D needle shapes, stiff tissue

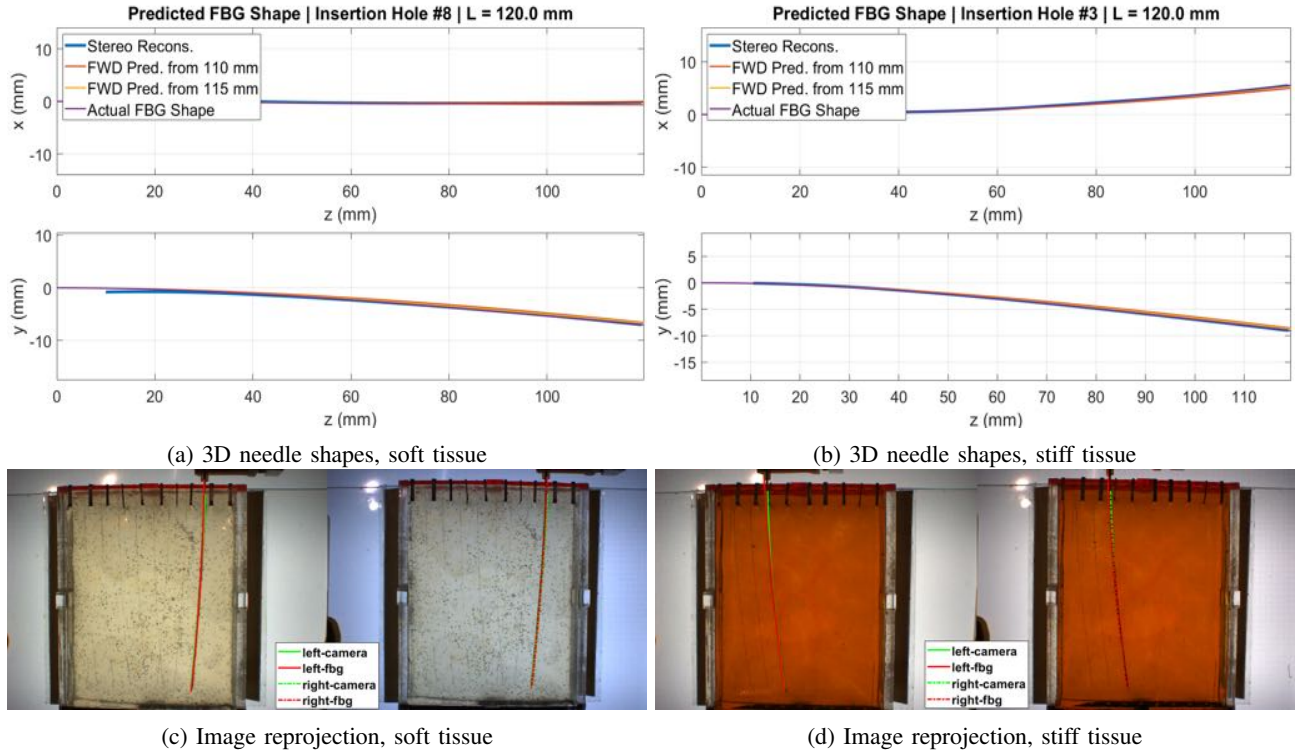|	
(c) Image reprojection, soft tissue	(d) Image reprojection, stiff tissue

Fig. 6: FBG-determined, predicted, and stereo ground truth 3D needle shapes at 120 mm insertion depth and the corresponding needle shape reprojections into the image plane for the soft and stiff tissues.

including prediction results from 110 and 115mm, and the image reprojections of the 3D needle shapes are illustrated for one of the soft and stiff tissue cases. Here, the stereo reconstruction is generally shown shorter than the FBG-determined needle shape due to loss of visualization and difficulty of segmentation of the needle at the insertion point of the needle into the tissue. Therefore, in order to compute deviations between the stereo reconstructed and FBG-determined needle shapes, we compare the needle shapes only for the overlapping sections.

Needle shape prediction was performed starting from 110 mm up to 120 mm, illustrated in Fig. 7b and Table II. We found over all trials, the mean RMSE for the FBG-

predicted shapes were 0.892 ± 0.389mm. In Fig. 6, we present the needle shape predictions from 110 and 115 mm to the measured shape at 120 mm. There are two outliers in each of the tissues found, caused by an error from the prediction at 110 mm to the 115 and 120 mm for a single insertion trial. This error is most likely attributed to errors in the sensor measurement, resulting in poor determination of κ_c and ω_{init}. After 110 mm, the errors were reduced and were of the typical distribution shown in Fig. 7b.

Our assumed model of κ_c's dependence from (5) was derived upon the assumption that the needle shape should not deviate upon increased insertion depths. From computational modelling, κ_c is expected to decrease over the deeper

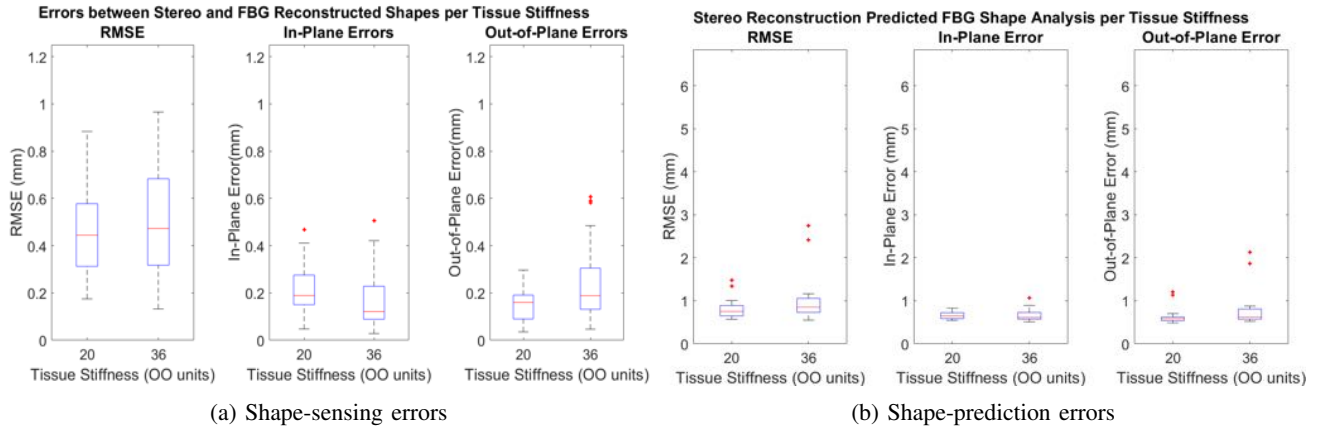(a) Shape-sensing errors   (b) Shape-prediction errors

Fig. 7: 3D needle shape-sensing and shape-prediction error results for each of the different tissue stiffnesses.

insertions; however, in Fig. 8, we see the exact opposite in the two individual insertions into soft and stiff tissue. This could potentially be due to increasing experienced loads on the needle upon further insertion. To better model the dependence of κ_c over the further insertion, we use our experimental results and fit a quadratic function of the form,

$$\frac{\kappa_c(L)}{\kappa_{c,ref}} = a\left(\frac{L}{L_{ref}} - 1\right)^2 + b\left(\frac{L}{L_{ref}} - 1\right) + 1, \quad (10)$$

where a and b are parameters to be fit optimally to $\kappa_c(L)$ from the two insertions into soft and stiff tissue. The a and b parameters were determined by a machine learning method, linear regression, to optimize a weighted least squares. Weighting was applied to the soft and stiff dataset according to the total amount of uncertainty present for the κ_c measurements, determined by the standard deviation over all of the insertion trials. The parameters determined were found to be: $a = -35.3967$ and $b = 7.9441$. Fig. 8 also shows the predicted κ_c values using the learned results from experimentally-determined κ_c over the insertion depths. This could potentially be used to refine the needle shape prediction, however, further exploration into this topic is required.

V. CONCLUSIONS

We presented and validated a sensor-based method for 3D needle shape-sensing and a novel method for 3D needle shape prediction for a four-active area FBG-sensorized needle in varying stiffness isotropic tissues using a single parameter for characterizing the change in the intrinsic curvature coefficient. We presented a method for 3D measurement of the needle shape using a stereo reconstruction during needle insertion in transparent tissue to serve as the ground truth. We proved that our model determines and predicts non-uniform 3D needle bending and curvatures through online estimation of the needle insertion mechanical parameters using FBG sensor readings. The results presented in this work demonstrate the validity of using a Lie-group theoretic approach to shape-sensing and shape-prediction in providing intraoperative feedback for needle insertions. A limitation of
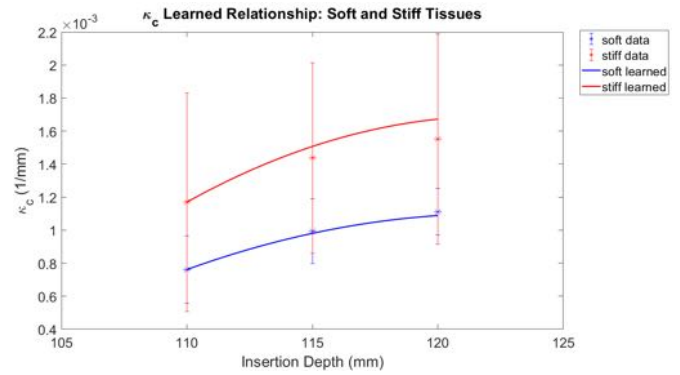

Fig. 8: Experimental values and learned function of κ_c over the insertion depths using machine learning for the soft and stiff tissues. The error bars from the experimental results are the standard deviation of κ_c over the insertion trials for the specified tissue and insertion depth.

this work is the experimental maximum insertion depth; this remains as a future work for characterizing the needle prediction model's prediction error over longer insertion depths. Also, the current experiment ensured that all sensors were inserted into the tissue. However, needle shape estimation and shape prediction can be performed prior to full insertion of the sensing locations in tissue; this remains as a future work. We also plan to explore multi-layer tissue scenarios and non-homogeneous, real tissue insertion experiments to further validate our needle shape sensing and prediction model in varying tissue configurations. Furthermore, we plan to study the dependence of κ_c on the insertion depth over longer insertions and apply machine learning methods to better improve our prediction of κ_c, thus, the predicted needle shape. Finally, the development of our prediction model founds our future work for accurate needle insertion planning methods used in needle steering.

ACKNOWLEDGMENT

References

[1] W. Park, J. S. Kim, Y. Zhou, N. J. Cowan, A. M. Okamura, and G. S. Chirikjian, "Diffusion-based motion planning for a nonholonomic flexible needle model," in *Proceedings of IEEE International Conference on Robotics and Automation*, 2005, pp. 4600–4605.

[2] R. J. Webster, J. S. Kim, N. J. Cowan, G. S. Chirikjian, and A. M. Okamura, "Nonholonomic modeling of needle steering," *International Journal of Robotics Research*, vol. 25, no. 5-6, pp. 509–525, 2006.

[3] R. Secoli and F. Rodriguez y Baena, "Closed-loop 3d motion modeling and control of a steerable needle for soft tissue surgery," in *2013 IEEE International Conference on Robotics and Automation*, 2013, pp. 5831–5836.

[4] M. Khadem, B. Fallahi, C. Rossa, R. S. Sloboda, N. Usmani, and M. Tavakoli, "A mechanics-based model for simulation and control of flexible needle insertion in soft tissue," *Proceedings - IEEE International Conference on Robotics and Automation*, vol. 2015-June, no. June, pp. 2264–2269, 2015.

[5] M. Khadem, C. Rossa, R. S. Sloboda, N. Usmani, and M. Tavakoli, "Mechanics of Tissue Cutting during Needle Insertion in Biological Tissue," *IEEE Robotics and Automation Letters*, vol. 1, no. 2, pp. 800–807, 2016.

[6] S. Jiang and X. Wang, "Mechanics-Based Interactive Modeling for Medical Flexible Needle Insertion in Consideration of Nonlinear Factors," *Journal of Computational and Nonlinear Dynamics*, vol. 11, no. 1, 01 2016, 011004. [Online]. Available: https://doi.org/10.1115/1.4030747

[7] J. S. Kim, J. Guo, M. Chatrasingh, S. Kim, and I. Iordachita, "Shape determination during needle insertion with curvature measurements," *IEEE International Conference on Intelligent Robots and Systems*, vol. 2017-Septe, pp. 201–208, 2017.

[8] J. S. Kim, M. Chatrasingh, and et. al, "Fiber bragg grating based needle shape sensing for needle steering system: Evaluation in inhomogeneous tissue," in *2017 IEEE SENSORS*, 2017, pp. 1–3.

[9] X. Jijie, V. Duindam, R. Alterovitz, and K. Goldberg, "Motion planning for steerable needles in 3D environments with obstacles using Rapidly-exploring random trees and backchaining," *4th IEEE Conference on Automation Science and Engineering, CASE 2008*, pp. 41–46, 2008.

[10] M. Li, D. Gao, Y. Lei, and T. Xu, "Dynamic Path Planning for Bevel-Tip Flexible Needle Insertion into Soft Tissue Based on a Real-Time Finite Element Model," *Mathematical Problems in Engineering*, vol. 2020, 2020.

[11] A. Wittek, G. Bourantas, B. F. Zwick, G. Joldes, L. Esteban, and K. Miller, "Mathematical modeling and computer simulation of needle insertion into soft tissue," *PLoS ONE*, vol. 15, 12 2020.

[12] D. A. Lezcano, I. I. Iordachita, and J. S. Kim, "Trajectory Generation of FBG-Sensorized Needles for Insertions into Multi-Layer Tissue," in *2020 IEEE Sensors*, 2020, pp. 1–4.

[13] J. S. Kim, M. Chatrasingh, S. Kim, J. Suthakorn, and I. I. Iordachita, "Fiber Bragg Grating based needle shape sensing for needle steering system: Evaluation in inhomogeneous tissue," *Proceedings of IEEE Sensors*, vol. 2017-Decem, no. c, pp. 1–3, 2017.

[14] G. Chirikjian and A. Kyatkin, *Harmonic Analysis for Engineers and Applied Scientists*. Dover, September 2015, (updated and expanded version of Engineering Applications of Noncommutative Harmonic Analysis, CRC Press, October 2000.).

[15] D. D. Holm, J. E. Marsden, and T. S. Ratiu, "The Euler-Poincaré equations and semidirect products with applications to continuum theories," *Advances in Mathematics*, vol. 137, pp. 1–81, 1998.

[16] J. S. Kim and G. S. Chirikjian, "Conformational analysis of stiff chiral polymers with end-constraints," *Molecular Simulation*, vol. 32, pp. 1139 – 1154, 2006.

[17] L. Zhang, C. Li, X. Zhang, G. Liu, Y. Liu, J. Zhao, G. Ban, and Y. Fan, "A new method for fiber bragg grating based needle shape sensing calibration," in *2019 IEEE International Conference on Robotics and Biomimetics (ROBIO)*, 2019, pp. 1953–1958.